Opto-Electronic Science

CN 51-1800/O4 ISSN 2097-0382 (Print) ISSN 2097-4000 (Online)

Efficient generation of vectorial terahertz beams using surface-wave excited metasurfaces

Zhuo Wang, Weikang Pan, Yu He, Zhiyan Zhu, Xiangyu Jin, Muhan Liu, Shaojie Ma, Qiong He, Shulin Sun and Lei Zhou

Citation: Wang Z, Pan WK, He Y, et al. Efficient generation of vectorial terahertz beams using surface-wave excited metasurfaces. *Opto-Electron Sci* **4**, 240024 (2025).

https://doi.org/10.29026/oes.2025.240024

Received: 3 September 2024; Accepted: 11 November 2024; Published online: 15 January 2025

Opto-Electronic Science

Article

January 2025, Vol. 4, No. 1

DOI: 10.29026/oes.2025.240024 CSTR: 32246.14.oes.2025.240024

Efficient generation of vectorial terahertz beams using surface-wave excited metasurfaces

Zhuo Wang[1†], Weikang Pan[2†], Yu He[1], Zhiyan Zhu[2], Xiangyu Jin[2], Muhan Liu[2], Shaojie Ma[2], Qiong He[1,3], Shulin Sun[2,3,4*] and Lei Zhou[1,3*]

On-chip devices for generating pre-designed vectorial optical fields (VOFs) under surface wave (SW) excitations are highly desired in integrated photonics. However, conventional devices are usually of large footprints, low efficiencies, and limited wave-control capabilities. Here, we present a generic approach to design ultra-compact on-chip devices that can efficiently generate pre-designed VOFs under SW excitations, and experimentally verify the concept in terahertz (THz) regime. We first describe how to design SW-excitation metasurfaces for generating circularly polarized complex beams, and experimentally demonstrate two meta-devices to realize directional emission and focusing of THz waves with opposite circular polarizations, respectively. We then establish a systematic approach to construct an integrated device via merging two carefully designed metasurfaces, which, under SW excitations, can separately produce pre-designed far-field patterns with different circular polarizations and generate target VOF based on their interference. As a proof of concept, we demonstrate experimentally a meta-device that can generate a radially polarized Bessel beam under SW excitation at ~0.4 THz. Experimental results agree well with full-wave simulations, collectively verifying the performance of our device. Our study paves the road to realizing highly integrated on-chip functional THz devices, which may find many applications in biological sensing, communications, displays, image multiplexing, and beyond.

Keywords: surface waves; vector beam; multi-pixel metasurface; terahertz; ultrathin and high-efficiency

Wang Z, Pan WK, He Y et al. Efficient generation of vectorial terahertz beams using surface-wave excited metasurfaces. *Opto-Electron Sci* **4**, 240024 (2025).

Introduction

Propagating waves (PWs) and surface waves (SWs)[1] (including surface plasmons and their low-frequency counterpart spoof surface plasmons) are two distinct modes of electromagnetic (EM) waves. Controlling both of them in pre-designed manners is highly desirable for photonics applications[2–9]. Traditionally, diffractive optical elements are used to scatter PWs to achieve certain functionalities (say, light bending, imaging, etc.). However, these systems are typically too bulky in size, making them unsuitable for optical integrations[10–12]. In parallel, significant efforts have been devoted to employing on-chip devices to control SWs, leading to fascinating applications such as photonic circuits[13], light concentration[14–18],

[1]State Key Laboratory of Surface Physics and Key Laboratory of Micro and Nano Photonic Structures (Ministry of Education), Fudan University, Shanghai 200433, China; [2]Shanghai Engineering Research Centre of Ultra Precision Optical Manufacturing, Department of Optical Science and Engineering, School of Information Science and Technology, Fudan University, Shanghai 200433, China; [3]Shanghai Key Laboratory of Metasurfaces for Light Manipulation, Shanghai 200433, China; [4]Yiwu Research Institute of Fudan University, Chengbei Road, Yiwu City 322000, China.

†These authors contributed equally to this work.

*Correspondence: SL Sun, E-mail: sls@fudan.edu.cn; L Zhou, E-mail: phzhou@fudan.edu.cn

Received: 3 September 2024; Accepted: 11 November 2024; Published online: 15 January 2025

quantum photonics[19], optical computing[20], etc. Recently, ultra-compact planar devices that can efficiently link PWs and SWs have attracted intensive attention, further enriching our abilities to control EM waves[21,22]. In particular, on-chip devices capable of generating pre-designed complex far-field patterns under SW excitations are highly sought after for various application scenarios[23–25] (say, virtual-reality displays, plasmonic nano-lasers, etc.). Available devices for these applications are usually plasmonic metals drilled with a series of slots arranged in particular sequences; each slot can scatter incident SWs to free-space PWs via introducing reciprocal vector, and thus their interferences can form the target far-field patterns[26–33]. However, these devices usually exhibit relatively low working efficiencies and limited functionalities, since the adopted working principles are similar to the Bragg-scattering mechanism, which suffers from multimode diffractions and difficulties in generating complex field patterns with fine internal features.

Metasurfaces (MSs), ultrathin metamaterials composed of deep-subwavelength microstructures (i.e., meta-atoms) with tailored optical responses arranged in certain global sequences, exhibit extraordinary capabilities for controlling EM waves[34–38]. Many fascinating wave-manipulation effects have been demonstrated with MSs possessing carefully designed phase profiles, such as anomalous refraction and reflection[34–36,39–41], meta-lens imaging[42–45], meta-holograms[46–48], optical logic gates[49] and so on. In particular, carefully designed gradient MSs can serve as efficient couplers to convert free-space EM waves into SWs, in which their phase gradients can compensate for the momentum mismatch between PWs and SWs. By adding additional phase terms to the phase profiles, many functional meta-couplers have been demonstrated in different frequency domains, that can convert incident PWs into SWs exhibiting tailored wavefronts[36,50–54]. On the other hand, MSs that can decouple SWs into PWs have also attracted research interests recently[55–59]. In particular, a few on-chip meta-devices were designed with phase profiles governed by Pancharatnam-Berry (PB) mechanism[56–58,60], which can decouple the incident SWs into spin-polarized PWs with tailored wavefronts. Table S1 summarizes the key features of our work in comparison with previous literature (see Section 1 in Supplementary information). We find that most previously realized SW-excited metadevices exhibit quite low efficiencies, without optimizing the constitutive meta-atoms to considering the balance between wavefront flatness and efficiency. Meanwhile, most SW-excited meta-devices are realized in either optical or microwave regimes, while those for generating vectorial optical fields (VOFs) in the THz regime are particularly rare.

In this work, we establish a systematic approach to design on-chip devices that can efficiently decouple incident SWs into pre-designed VOFs in the FF, and experimentally verify the concept in the THz frequency domain. We first recap the design principles for constructing on-chip MSs to achieve single spin-polarized FF beams under SW excitations, and experimentally demonstrate two THz meta-devices as the proof of concept. Specifically, under the excitations of an incident SW beam at ~0.4 THz, the first device can generate a left-circular-polarization (LCP) beam propagating in a pre-designed direction with a relative efficiency of 95%, while the second device focuses a right-circular-polarization (RCP) beam to a specific FF point with a relative efficiency of 90%. Based on these benchmark results, we then establish a generic approach to design VOF-generation meta-devices by "merging" two MSs together, each producing a pre-designed FF pattern with a specific circular polarization under identical SW excitation. The interference of two spin-polarized FF beams leaking out of the device forms the target VOF. We follow this strategy to design and fabricate a VOF-generation meta-device and experimentally demonstrate that it can generate a radially polarized THz Bessel beam under the excitation of a THz SW at ~0.4 THz. Near-field scanning experiments are performed to characterize the generated THz VOF, and the results are in good agreement with full-wave simulations.

Results and discussions

Physical concept and design strategy

We first introduce our strategy for constructing a MS, which, under the excitation of a SW with frequency ω and wavevector

$$k_{\mathrm{SW}} > k_0 = \frac{\omega}{c},$$

can generate a spin-polarized FF beam characterized by a k-space distribution $E_\sigma(\boldsymbol{k})$. Here, $\sigma = +1$ represents LCP and $\sigma = -1$ represents RCP, respectively. Suppose that the phase distribution of a planar source to generate the target FF beam is $\varphi^{\mathrm{tar}}(\boldsymbol{r})$, obtained through analytical methods or computer-generated-hologram retrieval. Then, the phase distribution of our MS $\varphi_\sigma^{\mathrm{MS}}(\boldsymbol{r})$ should satisfy:

$$k_{\mathrm{SW}} \cdot x + \varphi_{\sigma}^{\mathrm{MS}}(\boldsymbol{r}) = \varphi^{\mathrm{tar}}(\boldsymbol{r}) \ , \tag{1}$$

derived from Huygens' principle. Here $k_{\mathrm{SW}} \cdot x$ represents the additional phase contributed by the excitation SW beam flowing along the x direction.

We construct our MS based on the PB mechanism, as the beam being generated is spin-polarized. With the desired phase distribution $\varphi_{\sigma}^{\mathrm{MS}}(\boldsymbol{r})$ determined by solving Eq. (1), we then employ a series of identical meta-atoms to construct our MS, with the meta-atoms located at the position $\boldsymbol{r}$ exhibiting the rotation angle:

$$\alpha(\boldsymbol{r}) = \varphi_{\sigma}^{\mathrm{MS}}(\boldsymbol{r})/2\sigma. \tag{2}$$

In general cases where the meta-atom does not exhibit a 100% polarization conversion ratio (PCR), the waves scattered by such a meta-atom contain both a spin-converted anomalous mode with a PB phase and a spin-maintained normal mode without any phase retardation. Given that the excitation beam is now a linearly-polarized SW rather than a circularly polarized beam, we understand that such a MS should, in principle, generate three beams: two anomalous modes with the desired spin σ and the undesired spin $-\sigma$, respectively, and one linearly polarized normal mode.

We now argue that only the beam with the desired spin can survive, since the excitation field is a SW. When the MS is shined by a normally incident linearly polarized beam (Fig. 1(a)), three beams can indeed be generated simultaneously in the FF. They correspond to sources with phase distributions $\{\varphi_{\sigma}^{\mathrm{MS}}(\boldsymbol{r}), -\varphi_{\sigma}^{\mathrm{MS}}(\boldsymbol{r}), \varphi_{\mathrm{N}}^{\mathrm{MS}}(\boldsymbol{r}) = 0\}$, respectively. The anomalous mode with the desired (undesired) spin propagates to the left (right) side of the normal. As the incident angle θ increases, each generated beam gains an additional tangential wave-vector $-k_x$ and is thus tilted to the right (Fig. 1(b)). In the extreme case where the excitation beam is a SW, both the normal beam and the undesired anomalous beam become evanescent waves bounded on the MS, and only the desired anomalous mode can be decoupled to the FF (see Fig. 1(c)). Here, we assume that the anomalous beam generated by the MS is a paraxial beam, with its maximum $-k_x$ component suppressed to an evanescent mode after the phase term $k_{\mathrm{SW}} \cdot x$ is added.

Based on these preparations, we are ready to establish a generic approach for designing a SW MS to generate a pre-designed FF vectorial beam. Given an arbitrary FF vectorial beam described by a momentum-space distribution $\boldsymbol{E}_{\mathrm{tar}}(\boldsymbol{k})$, we can always decouple it as $\boldsymbol{E}_{\mathrm{tar}}(\boldsymbol{k}) = E_{+}(\boldsymbol{k})|+\rangle + E_{-}(\boldsymbol{k})|-\rangle$ where $|\pm\rangle$ represent two orthogonal spin states, respectively. In principle, these spin states depend on the wavevector $\boldsymbol{k}$. Under the paraxial limit, we can neglect these dependences and replace them by the spin states corresponding to the central wavevectors. Therefore, the target field under construction can now be formally expressed as:

$$\begin{aligned}\boldsymbol{E}_{\mathrm{tar}}(\boldsymbol{r}) &= \int \boldsymbol{E}_{\mathrm{tar}}(\boldsymbol{k})\, \mathrm{e}^{\mathrm{i}\boldsymbol{k}\cdot\boldsymbol{r}}\mathrm{d}\boldsymbol{k} \\ &= \int \{E_{+}(\boldsymbol{k})|+\rangle + E_{-}(\boldsymbol{k})|-\rangle\}\, \mathrm{e}^{\mathrm{i}\boldsymbol{k}\cdot\boldsymbol{r}}\mathrm{d}\boldsymbol{k} \ ,\end{aligned} \tag{3}$$

where $E_{+}(\boldsymbol{k})$ and $E_{-}(\boldsymbol{k})$ describe the momentum-space

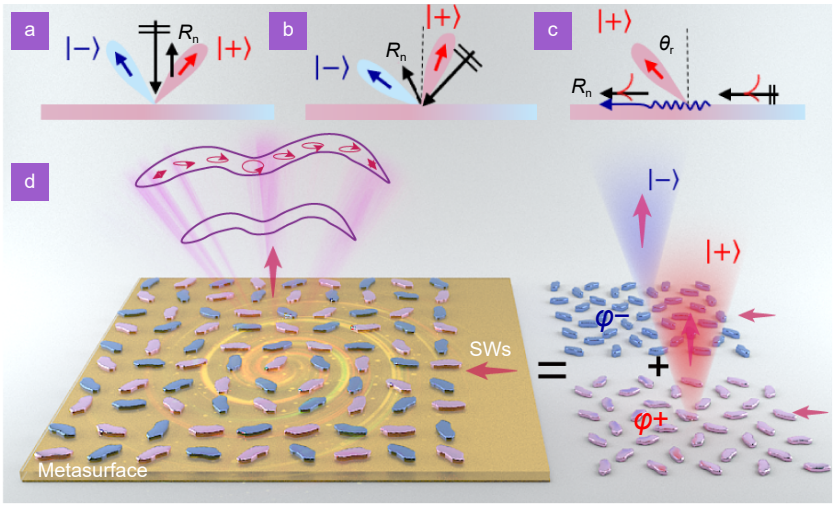

Fig. 1 | Schematic illustrations of working mechanism and vectorial light field generation by the proposed SW MS. (**a**, **b**) Schematics of mulitiple mode generation by a PB MS illuminated by linearly polarized free-space light with different incident angles. (**c**) Schematic of single mode radiation with the specific spin state by a PB MS illuminated by SW. (**d**) Schematic of the complex vectorial light field radiation created by a multi-pixel MS capable of decoupling both LCP and RCP components with well-controlled phase difference, under excitation of impinging SWs.

distributions of two circularly polarized FF beams with opposite spins.

Now the design strategy is very clear. First, we design two MSs that, under the same SW excitations, can respectively generate two spin-polarized FF beams characterized by momentum-space distribution $E_+(\boldsymbol{k})$ and $E_-(\boldsymbol{k})$. Next, we "merge" these two MSs together to form our final meta-device (see Fig. 1(d)). As being excited by the SW, each part of the meta-device can generate a pre-designed FF beam with a particular spin, and the interference between these two spin-polarized beams in the FF forms the desired FF VOF (see Eq. (2)). To avoid structural overlapping in the "merging" process, we arrange the meta-atoms belonging to one MS in a checkboard pattern occupying only half of the whole area (see Fig. 1(d)).

At the end of this subsection, we address several issues. Usually, PB meta-atoms with the highest possible PCRs are preferred in designing PB meta-devices under PW excitation because the strengths of the anomalous modes generated by these devices are proportional to the PCRs of constituent meta-atoms[61,62]. However, the situation is quite different when designing a SW MS. As the source SW flows across all meta-atoms within the device, its field strength inevitably decays due to decoupling to the FF by the anomalous mode. Consequently, the meta-atoms at different positions experience excitation fields of varying strengths. Such inhomogeneity in excitation-field can cause wave-front non-flatness, significantly degrading the quality of the generated beam. To avoid this issue, here low-PCR meta-atoms are purposely designed, as the scattering by a meta-atom only weakly perturb the strength of SW. Moreover, adopting low-PCR meta-atoms does not necessarily mean that the device exhibits a low efficiency. As shown in Fig. 1(c), only the desired anomalous mode can be decoupled from the MS, while the other two modes remain as evanescent waves that cannot leave the MS. Energy carried by these two evanescent modes is eventually returned to the source SW through multiple scatterings and are not wasted ultimately. Thus, PCR of constitutional meta-atom actually characterizes the decoupling speed of the constructed meta-device. Therefore, a device composed of meta-atoms with lower PCR should exhibit a larger effective aperture size in order to help well construct complex FF excited by the SW. We numerically examined how the PCR values of meta-atoms affect the performances of PB meta-devices under excitations of PWs and SWs, respectively, and found these two cases exhibit distinct behaviors (see Section 2 of Supplementary information for more details).

Design and characterizations of the PB meta-atom

We now design an appropriate meta-atom for constructing the THz meta-devices demonstrated in this paper and experimentally characterize its scattering properties. Considering a generic reflective meta-atom with mirror-reflection symmetry, we can describe its scattering properties using a Jones matrix $\boldsymbol{R}=\begin{bmatrix} r_{uu} & 0 \\ 0 & r_{vv} \end{bmatrix}$, where u and v denote two principal axes of the structure. Ignoring material losses and assuming the meta-atom is totally reflective, we can rewrite two reflection coefficients as $r_{uu}=\mathrm{e}^{\mathrm{i}\varphi_{uu}}$ and $r_{vv}=\mathrm{e}^{\mathrm{i}\varphi_{vv}}$ with φ_{uu} and φ_{vv} describing the reflection phases for incident THz beams with different linear polarizations. We note that PCR of the meta-atom is defined as $PCR=|r_{uu}-r_{vv}|^2/4=|\mathrm{e}^{\mathrm{i}\Delta\varphi}-1|^2/4$, which is closely related to the phase difference $\Delta\varphi=\varphi_{uu}-\varphi_{vv}$. Therefore, our task is to design a meta-atom with an appropriate $\Delta\varphi$ that yields a reasonably low PCR, suitable for designing our meta-devices with fixed total sizes.

As shown in the inset to Fig. 2(a), our meta-atom is in a metal-insulator-met (MIM) configuration, consisting of a gold nano-bar and a continuous 60 nm-thick gold film separated by a 60 μm -thick quartz spacer (ε = 3.9). Choosing the working frequency as 0.4 THz, we carefully optimize the meta-atom structure using finite-difference time-domain (FDTD) simulations and fix the structural parameters as: p=166.6 μm, L=132 μm, W=23.5 μm. We fabricate a sample consisting of a periodic array of the designed meta-atoms using optical lithography and use THz time-domain spectroscopy (TDS) to characterize its optical properties. Since the bottom gold mirror completely blocks the transmission channel, we only need to measure the reflection spectrum of the sample. Figure 2(b) shows the measured spectra of reflection amplitudes and phase difference of the sample under illumination by THz light beams polarized along u- and v-axes, respectively. While the measured reflection amplitudes remain at high values, the phase difference $\Delta\varphi$ varies significantly with frequency. With both reflection amplitudes and phases measured, we then calculate the generation efficiencies of the normal mode ($R_\mathrm{n}=|r_{uu}+r_{vv}|^2/4$) and the anomalous one ($R_\mathrm{a}=|r_{uu}-r_{vv}|^2/4$) for the fabricated PB meta-atom, and depict the results in Fig. 2(c). We find that R_a

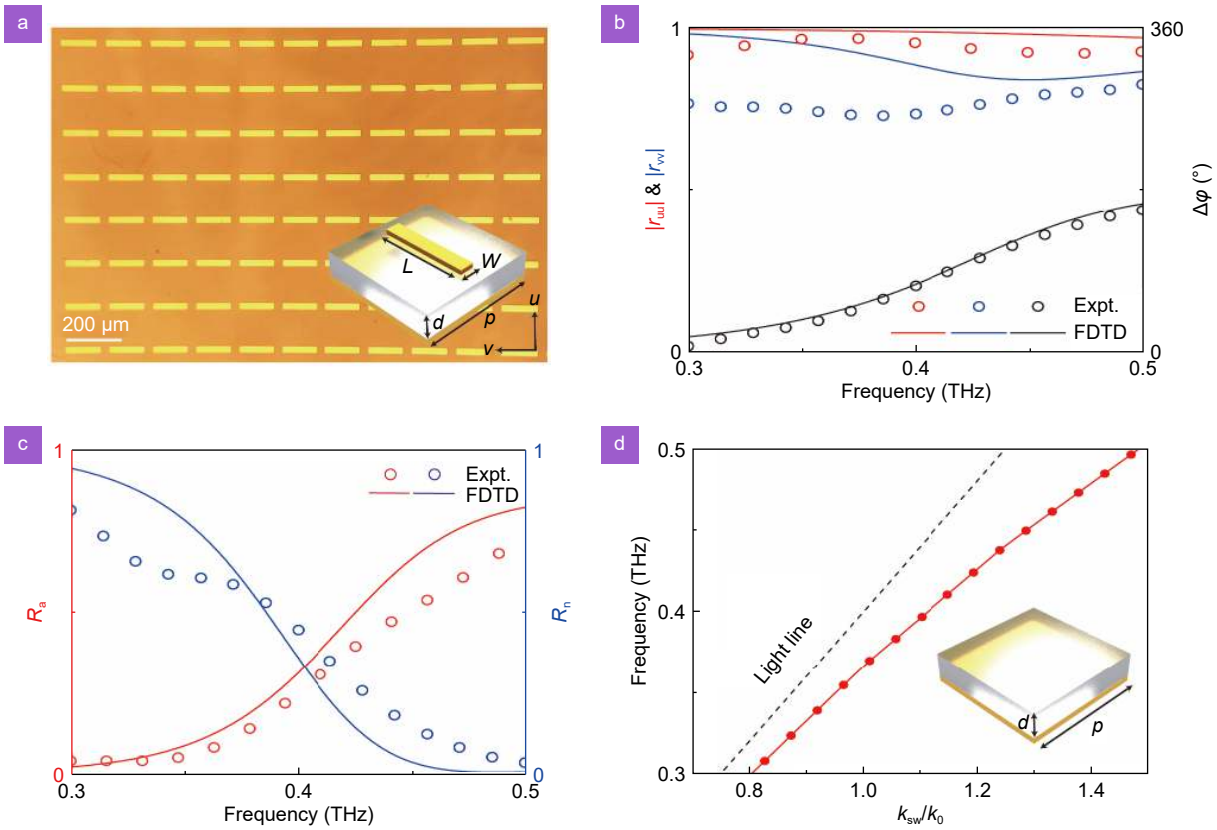

Fig. 2 | Design and characterization of the PB meta-atom and plasmonic metal. (**a**) The sample image of the proposed metal-insulator-metal typed meta-atoms arranged in a periodic array with the geometry shown in the inset. Here, p = 166.6 μm, L = 132 μm, W = 23.5 μm, and d = 60 μm. (**b**) The reflection amplitudes $|r_{uu}|$, $|r_{vv}|$ and phase difference $\Delta\varphi = \varphi_{uu} - \varphi_{vv}$ of the meta-atoms illuminated by the terahertz light linearly polarized along the two principle axes, i.e., u and v axes, obtained by both simulations and experiments. (**c**) The retrieved efficiency of normal and abnormal reflection modes (R_n and R_a) based on the data in (b). (**d**) Simulated dispersion relation of eigen SW modes supported by the designed plasmonic metal.

increases from 0 to 0.9 as frequency changes from 0.3 to 0.5 THz, which is consistent with the measured $\Delta\varphi$ spectrum as shown in Fig. 2(b). At the operating frequency of 0.4 THz, we get $R_a = 0.32$ which is quite reasonable for our designs (see Supplementary Section 3). All experimental results are in good agreement with the corresponding FDTD simulations.

We further design a "plasmonic metal" that supports appropriate SWs, serving as a platform to inject the source SW. To minimize scattering at the interface between the "plasmonic metal" and the MS, we purposely choose the "plasmonic metal" as a 60 nm-thick continuous gold layer capped with a 60 μm-thick quartz layer, which is identical to the bottom structure of the MS. Figure 2(d) depicts the computed dispersion relation of the SWs (e.g., spoof surface plasmons) supported by the "plasmonic metal", from which we find that $k_{SW} = 1.14k_0$ at 0.4 THz.

Benchmark tests: SW meta-devices for achieving spin-polarized FF beams

As the benchmark tests of our proposed concept and necessary preparations for constructing the VOF-generation devices, we first experimentally demonstrate two MSs that, under SW excitations at 0.4 THz, can generate unidirectional radiation and focusing of THz beams in the FF, exhibiting LCP and RCP, respectively.

The first meta-device is designed to generate directional radiation at the angle of $\theta_r = -45°$, as shown in Fig. 3(a). With the target FF beam known, we can analytically retrieve the target phase distribution as $\Phi^{tar}(\boldsymbol{r}) = \Phi_0 - k_0 \sin\theta_r x$, where Φ_0 is an arbitrary initial constant. Substituting $\Phi^{tar}(\boldsymbol{r})$ into Eq. (1), we find that the PB meta-device should exhibit the following reflection-phase distribution for LCP light at 0.4 THz:

$$\Phi_+(x) = \Phi_0 + k_0 \sin\theta_r x - k_{SW} x = \Phi_0 + 0.43k_0 \cdot x\,. \quad (4)$$

Substituting Eq. (4) into Eq. (2), we get the rotation-

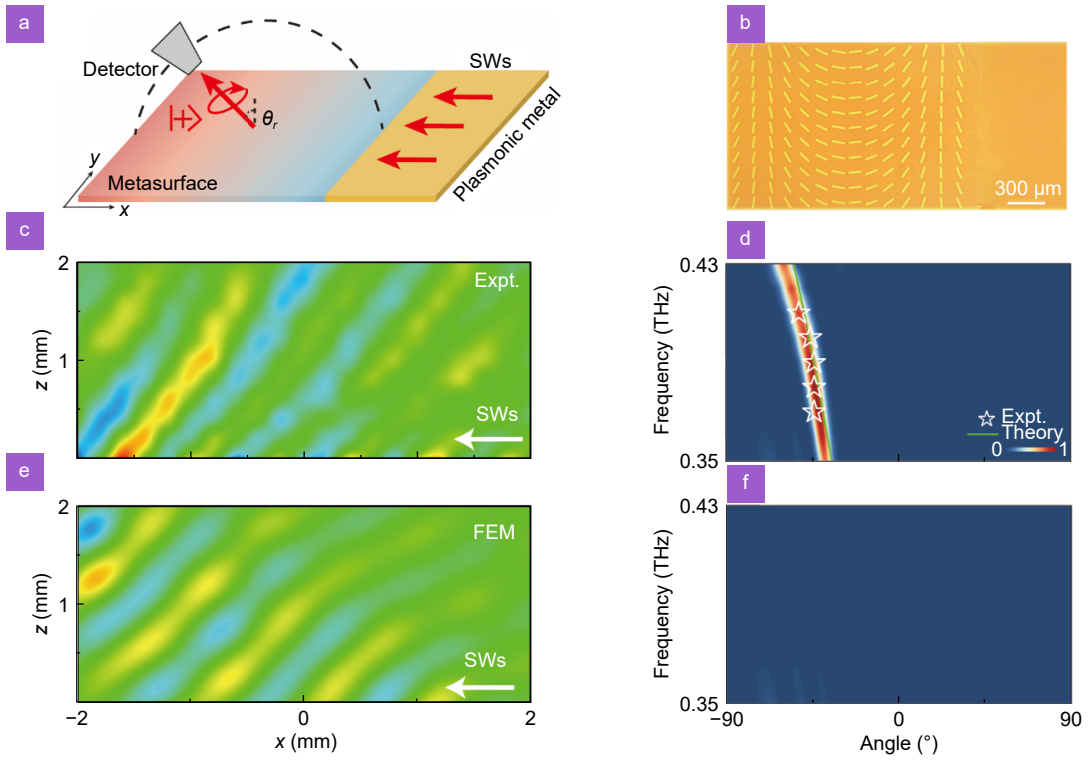

Fig. 3 | Near-field mapping and far-field angle-resolved characterization of SW-PW unidirectional radiation. (**a**, **b**) Schematic illustration and sample picture of the on-chip metadevice with the MS and plasmonic metal jointed together to achieve unidirectional spin-polarized far-field radiation of SWs. (**c**, **e**) Measured and simulated electric field Re(E_y) distributions on the *xz* plane of the MS excited by the near-field SWs launched along −*x* direction at 0.4 THz. (**d**, **f**) Scattered electric field intensity (color map) carrying LCP and RCP of the MS at different radiation angles and frequencies.

angle distribution of our meta-atoms, and fabricate the sample according to the design, which consists of both the MS and an adjacent "plasmonic metal", with an optical image shown in Fig. 3(b).

We now experimentally characterize the functionality of our fabricated meta-device. By launching an SW beam propagating along the $-x$ direction via shining a meta-coupler placed at the right-hand side of the "plasmonic metal" (see more information in Supplementary Section 4) at 0.4 THz (see Fig. 3(a)), we adopt the THz near-field (NF) scanning technology to characterize the scattered-field distribution on the *x*-*z* plane across the center of meta-device (see Section 5 of Supplementary information for more details). Measured Re(E_y) pattern depicted in Fig. 3(c) clearly shows that a beam propagating along the −45° direction has been formed. We further employ a THz angle-resolved TDS system to characterize the spin-dependent performance of the meta-device. In our measurements, under SW excitations at different frequencies, we adopt an NF probe to detect two orthogonal components of scattered electric fields (i.e., $E_{x'}$ and $E_{y'}$ where *x*' and *y*' denoting two local axes) at different angles, obtained by rotating the detector on a motorized stage. Transforming the measurement data into electric-fields in CP bases (i.e., $E^{\sigma} = (E_{x'} - \mathrm{i}\sigma E_{y'})/\sqrt{2}$), we then obtain the angular distributions of LCP and RCP components of the scattered electric fields at different frequencies. Fig. 3(d) and 3(f) show clearly that the scattered field contains only LCP component and no RCP signals can be measured. Experimentally measured peak-signal angles are represented by stars in Fig. 3(d) at different frequencies, which agree well with finite element method (FEM) simulations (color map) and theoretical predictions $\theta_r = \arcsin(-k_{\mathrm{SW}} - \mathrm{d}\Phi/\mathrm{d}x)$ according to Eq. (4) (green line). If the phase gradient is continuously varied from $-k_0 - k_{\mathrm{SW}}$ to $k_0 - k_{\mathrm{SW}}$, different far-field beams can be generated with radiation angles covering the full range of (−90°, +90°). We find that the scattered field is confined inside a narrow range centered at the predefined angle, consistent with our predictions that the generated beam is unidirectional one. Figure 3(d) shows that the PB meta-device works well within a broad frequency band, with the directional emission angle varying against frequency. From another point of view, the broad

frequency-band performance also implies that our meta-device can work for incident SWs taking wavevectors lying in a wide range. We employ FEM simulations to estimate the working frequency of our meta-device, which is defined as the ratio between the integrated power carried by the directional-emission beam and that of the incident SW. The absolute working efficiency reaches 60% (see Section 5 of Supplementary information for more details). If we exclude the energy absorbed by our meta-device from the incident energy, we can define a relative working efficiency, which reaches as high as 95%. Obviously, the main issue degrading the performance of our proposed metasurface is the Ohmic absorption, and the working efficiency can be further improved through introducing low-loss materials (e.g., dielectrics) into the structure design. This reinforces our previous argument that the meta-device is inherently efficient, as only one mode can be radiated out of the device.

We next demonstrate the second meta-device, which, under SW excitation at 0.4 THz, can generate an RCP beam decoupled from the device which is then focused to a point at a distance of $F = 2$ mm above the device (see Fig. 4(a)). To realize the target FF beam, we need to have a planar source exhibiting a phase distribution of $\Phi^{\rm tar} = \Phi_0 - k_0 \cdot (\sqrt{x^2+y^2+F^2} - F)$ with Φ_0 being an arbitrary constant. By substituting this equation into Eq. (1), we then retrieve the phase distribution of the meta-device under SW excitation as:

$$\Phi_{-}(x,y) = \Phi_0 - k_{\rm SW} \cdot x - k_0 \cdot (\sqrt{x^2+y^2+F^2} - F). \quad (5)$$

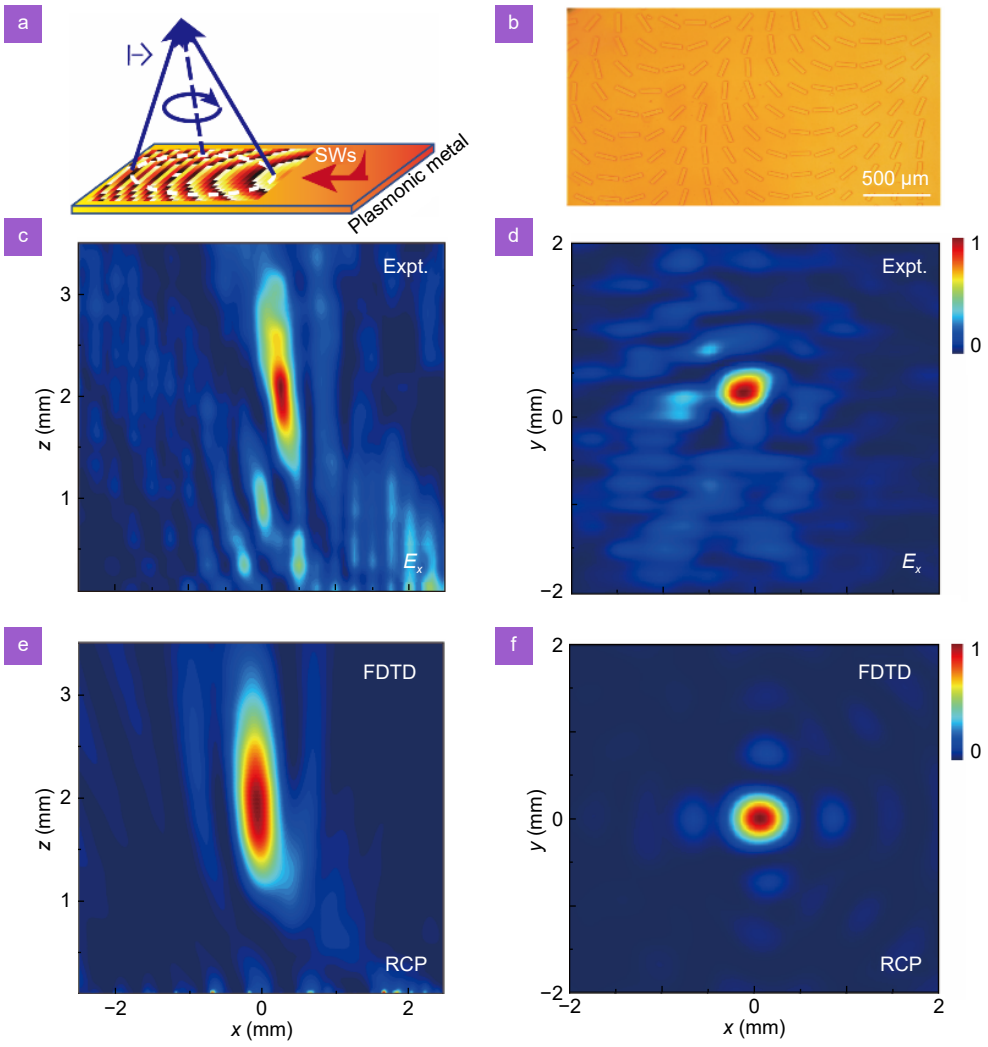

Fig. 4 | Characterization of far-field focusing of SW with the proposed on-chip meta-device. (**a**) Schematic of the SW-PW focusing with pre-defined spin state by the MS carrying specific geometric phase distribution. (**b**) Top-view picture of part of the fabricated MS sample. Measured (**c**, **d**), and simulated (**e**, **f**) electric field Re(E_x) distributions on the *xz* plane (*y*=0 mm) plane and the *xy* plane (*z*=2 mm) plane of the sample excited by SWs at 0.4 THz. In this case, all the fields are normalized to the corresponding maximum values in the patterns.

By substituting Eq. (5) to Eq. (2) to obtain the rotation-angle distribution of PB meta-atoms, we then complete the design and fabricate the sample. Again, the sample contains both the designed MS and a connecting "plasmonic metal" (see Fig. 4(b)). Employing the same experimental techniques as in Fig. 3, we measure electric-field distributions on both the *x*-*z* plane (z=100 μm) across the center of device and the *x*-*y* plane at z=2 mm, as the meta-device is excited by an SW at 0.4 THz launched from the right-hand side of the plasmonic metal. Figures 4(d) and 4(e) clearly show that a beam is decoupled from the MS and is then focused to the pre-designed focal point, as expected. FDTD-simulated electric-field patterns on these two planes are depicted in Fig. 4(f) and Fig. 4(g), respectively, agreeing well with their corresponding experimental counterparts (Fig. 4(d) and Fig. 4(e)). We have also employed FDTD simulations to calculate the relative efficiency of the device (with material losses excluded), and found it to be as high as 90%. Finally, we confirm that the polarized state of the generated beam is RCP by analyzing the scattered fields obtained in both measurements and simulations.

SW meta-device for generating a FF vectorial Bessel beam

Having completed all benchmark and preparation work in the last subsection, we now experimentally demonstrate a meta-device capable of generating a pre-designed VOF in the FF under SW excitation at 0.4 THz, following the general strategy described in Section *Physical concept and design strategy*. As schematically depicted in Fig. 5(a), the FF VOF that we aim to generate is a radially polarized Bessel beam with field distribution given by $\boldsymbol{E}_{\rm tar}(\boldsymbol{r},t)=E_0\cdot \mathrm{J}_1(k_\rho r)\left[\cos(\Phi)\,\hat{x}+\sin(\Phi)\,\hat{y}\right]\mathrm{e}^{\mathrm{i}k_z\cdot z}\mathrm{e}^{-\mathrm{i}\omega t}$ with $k_\rho{}^2+k_z{}^2=k_0{}^2$ and J_1 represents Bessel function. Obviously, the target VOF is radially polarized exhibiting no orbital angular momentum (OAM). By Fourier transforming the above expression in the FF to momentum space and then decoupling it into LCP and RCP bases according to Eq. (2), we find that

$$\begin{cases} E_+(\boldsymbol{k})=\dfrac{\mathrm{i}E_0}{\sqrt{2\pi}}\delta\left(\sqrt{k_x^2+k_y^2}-k_\rho\right) \\ E_-(\boldsymbol{k})=\dfrac{-\mathrm{i}E_0}{\sqrt{2\pi}}\delta\left(\sqrt{k_x^2+k_y^2}-k_\rho\right) \end{cases}. \tag{6}$$

Following the generic strategy described in Section *Physical concept and design strategy*, we need to first design two MS, which, under the same SW excitation, can generate a LCP beam with momentum-space distribution $\{E_+(\boldsymbol{k})\}$and a RCP beam with momentum-space distribution $\{E_-(\boldsymbol{k})\}$, respectively. Based on the design approach described in Section *Physical concept and design strategy* and the benchmark tests presented in Section *Benchmark tests: SW meta-devices for achieving spin-polarized FF beams*, we find that these two MSs should exhibit the following phase profiles:

$$\begin{cases} \Phi_+=-k_{\rm spp}x-k_0\rho\sin\theta_\rho+\phi \\ \Phi_-=-k_{\rm spp}x-k_0\rho\sin\theta_\rho-\phi+\pi \end{cases}, \tag{7}$$

where $\sqrt{x^2+y^2}=\rho$, $\varphi=\arctan(y/x)$ is the azimuthal angle. Equation (7) implies that two decoupled LCP and RCP Bessel beams with opposite OAM are generated, and their interference constructs the desired VOF with possessing a zero OAM (see original expression of the desired beam). We then retrieve the rotation-angle distributions of meta-atoms for these two MSs from Eq. (7) and merge them together to form the final target device. We note that the meta-atoms are carefully arranged to avoid overlapping with each other. Specifically, inside each supercell containing 4 meta-atoms, those at the upper-right and lower-left corners belong to MS 1, while the remaining two belong to MS 2. We fabricate the meta-device according to the design, which again contains both the MS and a connecting "plasmonic metal" (see Fig. 5(b)). We then perform THz near-field experiments to characterize the functionality of our fabricated meta-device. Figure 5(c) and 5(d) depict, respectively, the simulated and measured $|E_x|^2$ field patterns on the *x*–*z* plane with y=0, as the meta-device is excited by an SW at 0.4 THz flowing along the −*x* direction. Experimental results are in good agreement with FDTD simulations, clearly illustrating the non-diffraction property of the generated THz beam. We further experimentally characterize the vectorial nature of the generated beam. Using a LP detector with different orientations, we map out the patterns on the *x*-*y* plane with z=2 mm of the E-field polarized along different directions. Figure 5(e–h) show clearly that the recorded patterns change as the detector's orientation is rotated, unambiguously demonstrating that the generated THz beam is radially polarized. The simulation results are in excellent agreement with the experimentally measured ones (see Supplementary information Section 6).

Conclusions

We propose a general strategy to design meta-devices

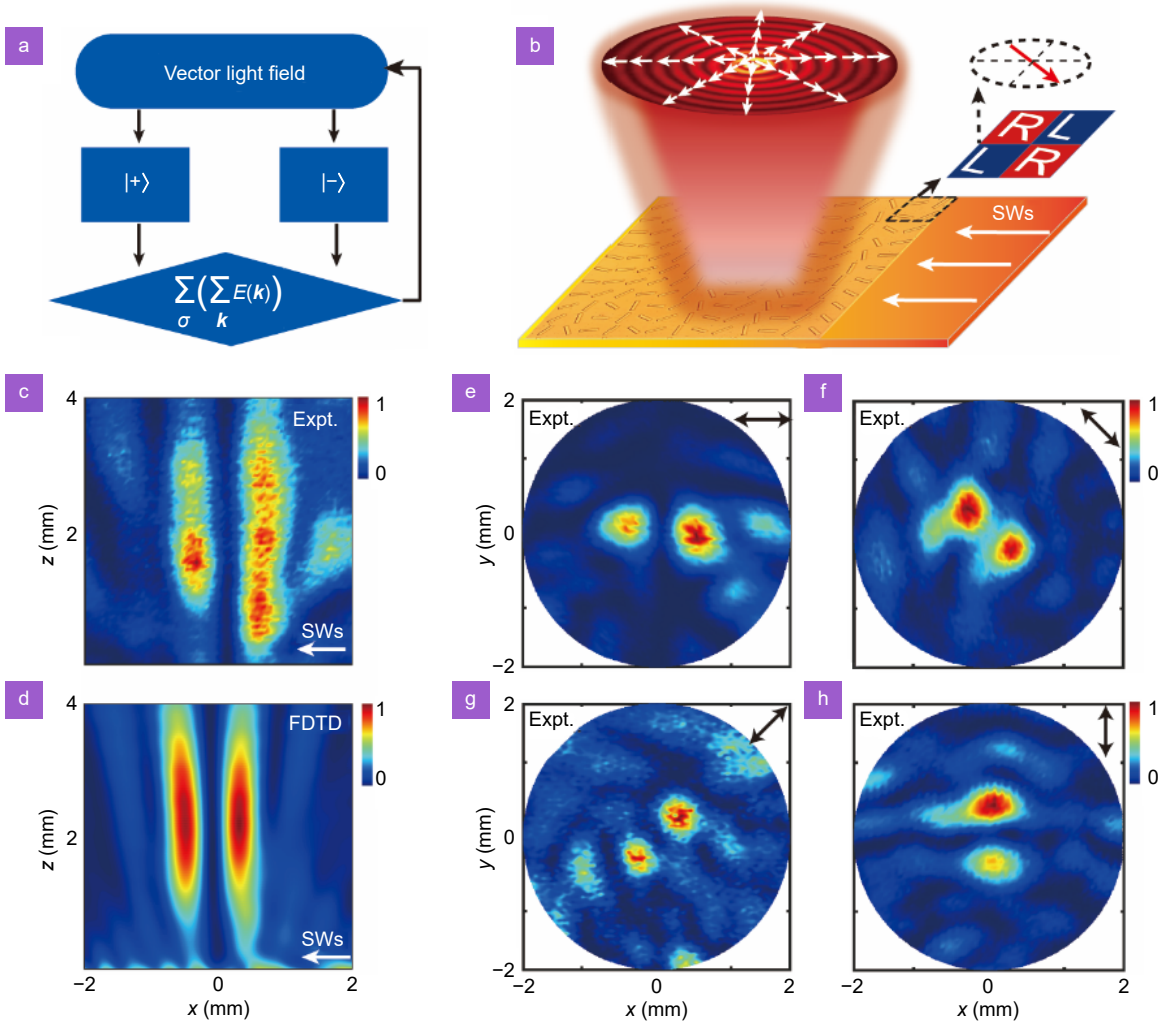

Fig. 5 | Vectorial Bessel beam generation with the on-chip THz multi-pixel MS. (**a**) Schematic of the design flowchart of the SW MS for creating complex vectorial FF. (**b**) Schematic of the conversion from SW to radially polarized Bessel FF beam. Part of the sample picture is shown as the inset in this figure. (**c**, **d**) Measured and simulated electric field $|E_x|^2$ intensity distribution on the *xz* plane (*y*=0 mm) when plane-wave like SWs at 0.4 THz enter the MS. (**e**–**h**) Measured electric field intensity distribution projected to the different linear polarization states of the generated vectorial Bessel beam on *xy* plane (*z*=2 mm) at 0.4 THz.

that, under certain SW excitations, can efficiently generate arbitrary pre-designed vectorial beams in the FF, and experimentally verify the concept in the THz regime. We first introduce how to design MSs to generate spin-polarized FF beams under SW excitations, and then establish the design strategy for constructing a VOF-generation meta-device by "merging" two MSs, which are separately designed for achieving the LCP and RCP components of the target VOF, respectively. After designing an appropriate constitutional meta-atom and experimentally characterizing its scattering properties, we use it to construct three devices and experimentally demonstrate their functionalities. Specifically, the first two devices are shown to generate a unidirectional LCP beam and an RCP beam focused to an FF point, while the third device can generate a cylindrically polarized Bessel beam, under the SW excitations at 0.4 THz. The experimentally measured results are in nice agreement with full-wave simulations. We emphasize that the proposed scheme is so general that it can be adopted to construct more complex vector holographic beams (see Supplementary Section 7). Our results establish a new ultra-compact platform for generating complex beams with arbitrary wavefronts and polarizations, which may inspire many integration-optics applications in different frequency domains.

References

1. Barnes WL, Dereux A, Ebbesen TW. Surface plasmon

subwavelength optics. *Nature* **424**, 824–830 (2003).
2. Fang N, Lee H, Sun C et al. Sub-diffraction-limited optical imaging with a silver superlens. *Science* **308**, 534–537 (2005).
3. Bozhevolnyi SI, Volkov VS, Devaux E et al. Channel plasmon subwavelength waveguide components including interferometers and ring resonators. *Nature* **440**, 508–511 (2006).
4. Gorodetski Y, Niv A, Kleiner V et al. Observation of the spin-based plasmonic effect in nanoscale structures. *Phys Rev Lett* **101**, 043903 (2008).
5. Zhao CL, Liu YM, Zhao YH et al. A reconfigurable plasmofluidic lens. *Nat Commun* **4**, 2305 (2013).
6. Richardson DJ, Fini JM, Nelson LE. Space-division multiplexing in optical fibres. *Nat Photonics* **7**, 354–362 (2013).
7. Fang YR, Sun MT. Nanoplasmonic waveguides: towards applications in integrated nanophotonic circuits. *Light Sci Appl* **4**, e294 (2015).
8. Guo XX, Ding YM, Chen X et al. Molding free-space light with guided wave–driven metasurfaces. *Sci Adv* **6**, eabb4142 (2020).
9. Li T, Chen C, Xiao XJ et al. Revolutionary meta-imaging: from superlens to metalens. *Photon Insights* **2**, R01 (2023).
10. Yamada I, Takano K, Hangyo M et al. Terahertz wire-grid polarizers with micrometer-pitch Al gratings. *Opt Lett* **34**, 274–276 (2009).
11. Scherger B, Jördens C, Koch M. Variable-focus terahertz lens. *Opt Express* **19**, 4528–4528 (2011).
12. Wei XL, Liu CM, Niu LT et al. Generation of arbitrary order Bessel beams via 3D printed axicons at the terahertz frequency range. *Appl Opt* **54**, 10641–10649 (2015).
13. Zia R, Schuller JA, Chandran A et al. Plasmonics: the next chip-scale technology. *Mater Today* **9**, 20–27 (2006).
14. Nie SM, Emory SR. Probing single molecules and single nanoparticles by surface-enhanced Raman scattering. *Science* **275**, 1102–1106 (1997).
15. Kim S, Jin J, Kim YJ et al. High-harmonic generation by resonant plasmon field enhancement. *Nature* **453**, 757–760 (2008).
16. Anker JN, Hall WP, Lyandres O et al. Biosensing with plasmonic nanosensors. *Nat Mater* **7**, 442–453 (2008).
17. Yu NF, Wang QJ, Kats MA et al. Designer spoof surface plasmon structures collimate terahertz laser beams. *Nat Mater* **9**, 730–735 (2010).
18. Kauranen M, Zayats AV. Nonlinear plasmonics. *Nat Photonics* **6**, 737–748 (2012).
19. Wang JW, Sciarrino F, Laing A et al. Integrated photonic quantum technologies. *Nat Photonics* **14**, 273–284 (2020).
20. Zhang H, Gu M, Jiang XD et al. An optical neural chip for implementing complex-valued neural network. *Nat Commun* **12**, 457 (2021).
21. Lalanne P, Hugonin JP, Rodier JC. Theory of surface plasmon generation at nanoslit apertures. *Phys Rev Lett* **95**, 263902 (2005).
22. López-Tejeira F, Rodrigo SG, Martín-Moreno L et al. Efficient unidirectional nanoslit couplers for surface plasmons. *Nat Phys* **3**, 324–328 (2007).
23. Li YZ, Zhang JX, Huang DD et al. Room-temperature continuous-wave lasing from monolayer molybdenum ditelluride integrated with a silicon nanobeam cavity. *Nat Nanotechnol* **12**, 987–992 (2017).
24. Kim SJ, Kang JH, Mutlu M et al. Anti-Hermitian photodetector facilitating efficient subwavelength photon sorting. *Nat Commun* **9**, 316 (2018).
25. Xiong JH, Hsiang EL, He ZQ et al. Augmented reality and virtual reality displays: emerging technologies and future perspectives. *Light Sci Appl* **10**, 216 (2021).
26. Lezec HJ, Degiron A, Devaux E et al. Beaming light from a subwavelength aperture. *Science* **297**, 820–822 (2002).
27. Shi HF, Du CL, Luo XG. Focal length modulation based on a metallic slit surrounded with grooves in curved depths. *Appl Phys Lett* **91**, 093111 (2007).
28. Kim S, Lim Y, Kim H et al. Optical beam focusing by a single subwavelength metal slit surrounded by chirped dielectric surface gratings. *Appl Phys Lett* **92**, 013103 (2008).
29. Piao XJ, Kumar MS, Koo S et al. High-efficiency out of plane conversion and manipulation of Surface Plasmon waves. In *Proceedings of the Digest of the 9th International Conference on Optical Internet* 8800–8805 (IEEE, 2010); http://doi.org/10.1109/COIN.2010.5546551.
30. Ozaki M, Kato JI, Kawata S. Surface-plasmon holography with white-light illumination. *Science* **332**, 218–220 (2011).
31. Chen YH, Huang L, Gan L et al. Wavefront shaping of infrared light through a subwavelength hole. *Light Sci Appl* **1**, e26 (2012).
32. Tang XM, Li L, Li T et al. Converting surface plasmon to spatial Airy beam by graded grating on metal surface. *Opt Lett* **38**, 1733–1735 (2013).
33. Chen J, Li T, Wang SM et al. Multiplexed holograms by surface plasmon propagation and polarized scattering. *Nano Lett* **17**, 5051–5055 (2017).
34. Yu NF, Genevet P, Kats MA et al. Light propagation with phase discontinuities: generalized laws of reflection and refraction. *Science* **334**, 333–337 (2011).
35. Ni XJ, Emani NK, Kildishev AV et al. Broadband light bending with plasmonic nanoantennas. *Science* **335**, 427 (2012).
36. Sun SL, He Q, Xiao SY et al. Gradient-index meta-surfaces as a bridge linking propagating waves and surface waves. *Nat Mater* **11**, 426–431 (2012).
37. He Q, Sun SL, Xiao SY et al. High-efficiency metasurfaces: principles, realizations, and applications. *Adv Opt Mater* **6**, 1800415 (2018).
38. Sun SL, He Q, Hao JM et al. Electromagnetic metasurfaces: physics and applications. *Adv Opt Photonics* **11**, 380–479 (2019).
39. Sun SL, Yang KY, Wang CM et al. High-efficiency broadband anomalous reflection by gradient meta-surfaces. *Nano Lett* **12**, 6223–6229 (2012).
40. Cui TJ, Qi MQ, Wan X et al. Coding metamaterials, digital metamaterials and programmable metamaterials. *Light Sci Appl* **3**, e218 (2014).
41. Xie X, Pu MB, Jin JJ et al. Generalized pancharatnam-berry phase in rotationally symmetric meta-atoms. *Phys Rev Lett* **126**, 183902 (2021).
42. Li X, Xiao SY, Cai BG et al. Flat metasurfaces to focus electromagnetic waves in reflection geometry. *Opt Lett* **37**, 4940–4942 (2012).
43. Chen XZ, Huang LL, Mühlenbernd H et al. Dual-polarity plasmonic metalens for visible light. *Nat Commun* **3**, 1198 (2012).
44. Aieta F, Kats MA, Genevet P et al. Multiwavelength achromatic metasurfaces by dispersive phase compensation. *Science* **347**, 1342–1345 (2015).
45. Wang SM, Wu PC, Su VC et al. Broadband achromatic optical metasurface devices. *Nat Commun* **8**, 187 (2017).

46. Chen WT, Yang KW, Wang CM et al. High-efficiency broadband meta-hologram with polarization-controlled dual images. *Nano Lett* **14**, 225–230 (2014).
47. Zheng GX, Mühlenbernd H, Kenney M et al. Metasurface holograms reaching 80% efficiency. *Nat Nanotechnol* **10**, 308–312 (2015).
48. Xiong B, Liu Y, Xu YH et al. Breaking the limitation of polarization multiplexing in optical metasurfaces with engineered noise. *Science* **379**, 294–299 (2023).
49. Krasikov S, Tranter A, Bogdanov A et al. Intelligent metaphotonics empowered by machine learning. *Opto-Electronic Adv* **5**, 210147 (2022).
50. Pors A, Nielsen MG, Bernardin T et al. Efficient unidirectional polarization-controlled excitation of surface plasmon polaritons. *Light Sci Appl* **3**, e197 (2014).
51. Sun WJ, He Q, Sun SL et al. High-efficiency surface plasmon meta-couplers: concept and microwave-regime realizations. *Light Sci Appl* **5**, e16003 (2016).
52. Duan JW, Guo HJ, Dong SH et al. High-efficiency chirality-modulated spoof surface plasmon meta-coupler. *Sci Rep* **7**, 1354 (2017).
53. Wang Z, Li SQ, Zhang XQ et al. Excite spoof surface plasmons with tailored wavefronts using high‐efficiency terahertz metasurfaces. *Adv Sci* **7**, 2000982 (2020).
54. Chen YZ, Zheng XY, Zhang XY et al. Efficient meta-couplers squeezing propagating light into on-chip subwavelength devices in a controllable way. *Nano Lett* **23**, 3326–3333 (2023).
55. Pan WK, Wang Z, Chen YZ et al. High-efficiency generation of far-field spin-polarized wavefronts via designer surface wave metasurfaces. *Nanophotonics* **11**, 2025–2036 (2022).
56. Fang B, Wang ZZ, Gao SL et al. Manipulating guided wave radiation with integrated geometric metasurface. *Nanophotonics* **11**, 1923–1930 (2022).
57. Huang HQ, Overvig AC, Xu Y et al. Leaky-wave metasurfaces for integrated photonics. *Nat Nanotechnol* **18**, 580–588 (2023).
58. Ji JT, Wang ZZ, Sun JC et al. Metasurface-enabled on-chip manipulation of higher-order poincaré sphere beams. *Nano Lett* **23**, 2750–2757 (2023).
59. Fang B, Fang B, Fang B et al. Spin-decoupled meta-coupler empowered multiplexing and multifunction of guided wave radiation. *Photonics Res* **11**, 2194–2201 (2023).
60. Zhao KY, Ha YL, Guo YH et al. On-chip integrated metasurface empowered multi-channel multiplexed three-dimensional hologram. *Adv Opt Mater* **12**, 2303009 (2024).
61. Luo WJ, Sun SL, Xu HX et al. Transmissive ultrathin pancharatnam-berry metasurfaces with nearly 100% efficiency. *Phys Rev Appl* **7**, 044033 (2017).
62. Luo WJ, Xiao SY, He Q et al. Photonic spin hall effect with nearly 100% efficiency. *Adv Opt Mater* **3**, 1102–1108 (2015).

Acknowledgements

The authors acknowledge the financial support from National Natural Science Foundation of China (Nos. 62192771, 12374344, 12221004), National Key Research and Development Program of China (2022YFA1204700, 2020YFA0710100), Natural Science Foundation of Shanghai (Grant No. 23dz2260100), China Postdoctoral Science Foundation 2021TQ0077. We acknowledge technical support from Fudan Nanofabrication Laboratory for sample fabrications.

Author contributions

Z.W. carried out the numerical calculations. Z.W. and W.K.P. performed the experiments. Y.H., X.Y.J., M.L., S.J.M., Q.H. contributed to the discussion of the manuscript. S.L.S., L.Z. conceived the project and wrote the manuscript.

Competing interests

The authors declare no competing financial interests.

Supplementary information

Supplementary information for this paper is available at
https://doi.org/10.29026/oes.2025.240024

Scan for Article PDF